Journal of Thermal Science Vol.30, No.1 (2021) 133−148

https://doi.org/10.1007/s11630-020-1242-1 **Article ID: 1003-2169(2021)01-0133-16**

Investigation on One-Dimensional Loss Models for Predicting Performance of Multistage Centrifugal Compressors in Supercritical CO_2 Brayton Cycle

SHAO Wenyang[1], DU Juan[2], YANG Jinguang[1*], WANG Xiaofang[1], LYU Guochuan[1]

1. School of Energy and Power Engineering, Dalian University of Technology, Dalian 116024, China
2. Institute of Engineering Thermophysics, Chinese Academy of Sciences, Beijing 100190, China

Abstract: The main compressor in a supercritical carbon dioxide (SCO_2) Brayton cycle works near the critical point where the physical properties of CO_2 are far away from the ideal gas. To investigate the effectiveness of the conventional one-dimensional (1D) loss models for predicting the performance of compressors working in such nontraditional conditions, detailed comparisons of 1D predicted performance, experimental data and three-dimensional CFD results are made. A 1D analysis method with enthalpy and total pressure based loss system is developed for multistage SCO_2 centrifugal compressors, and it is firstly validated against the experimental results of a single stage SCO_2 centrifugal compressor from the Sandia National Laboratory. A good agreement of pressure ratios with experiments can be achieved by the 1D method. But the efficiency deviations reveal the potential deficiencies of the parasitic loss models. On the basis of the validation, a two-stage SCO_2 centrifugal compressor is employed to do the evaluation. Three-dimensional CFD simulations are performed. Detailed comparisons are made between the CFD and the 1D results at different stations located in the compressor. The features of the deviations are analyzed in detail, as well as the reasons that might cause these deviations.

Keywords: supercritical carbon dioxide Brayton cycle, centrifugal compressor, one-dimensional performance analysis, loss model, three-dimensional CFD simulation

1. Introduction

In the modern world, most thermal power plants use steam as the working fluid to drive turbines. Steam-based generation produces 80% of the world's energy [1]. After more than a century of development and improvements, the steam thermal cycle has reached a relatively mature level. It seems to be difficult to achieve a remarkable efficiency improvement only by optimizing the design for the components working in the cycle. Therefore, new methods should be considered in order to further improve the thermal efficiency and reduce the CO_2 emission.

In recent years, the Supercritical Carbon Dioxide (SCO_2) Brayton cycle, which uses SCO_2 as working fluid, has received more and more attention [2]. Compared with the steam, higher density and gas-like viscosity of SCO_2 can significantly decrease the power consumed in compressors, especially when the inlet condition of the compressor is near the critical point. As a consequence, more mechanical energy generated by turbines could be transferred to electric power. In fact, the concept of SCO_2 Brayton cycle was firstly proposed and studied in the 1960s [3], but was discarded due to the limitations of industrial technology and manufacturing level. Recently,

Received: Nov 23, 2018 Corresponding author: YANG Jinguang E-mail: jinguang_yang@dlut.edu.cn

Nomenclature

A	passage area	ε	average size of the blade gap from impeller inlet to outlet
B	fractional area blockage	ε_w	wake fraction of the blade-to-blade space at impeller outlet
b	hub-to-shroud passage width	η	adiabatic efficiency
C_{fdf}	disk torque coefficient	ξ	enthalpy loss coefficient
c	absolute velocity	ϖ	total pressure loss coefficient
$\overline{c}$	mean absolute velocity	ϖ_{inc0}	minimum incidence loss coefficient
c_f	skin friction coefficient	ρ	fluid density
c_{slip}	slip velocity at impeller outlet	σ	slip factor
D_f	diffusion factor	ϕ	flow coefficient
d	diameter	**Subscripts**	
d_H	hydraulic diameter	0	total thermodynamic condition or stage inlet
h	enthalpy	1	impeller blade inlet
Δh	enthalpy loss	2	impeller outlet
Δh_{Euler}	impeller blade work	3	vaned diffuser inlet
I_{blade}	impeller blade work input coefficient	4	vaned diffuser outlet
L_b	length of blade mean camberline	6	crossover inlet
m	meridional coordinate	7	return channel vane trailing edge
$\dot{m}$	mass flow	cl	clearance gap
N	rotating speed	DIF	vaned diffuser
P	pressure	h	hub
r	radius	i	station number
SNL	Sandia National Laboratory	is	isentropic
T	temperature	m	meridional component
u	Circumferential speed	RC	return channel
w	relative velocity	t	tip
$\overline{w}$	mean relative velocity	th	throat
X	judgment criterion for the sonic condition	u	tangential component
Z	effective number of blades	**Superscripts**	
α	absolute flow angle from meridional	*	condition at minimum loss incidence angle
β	blade angle from meridional	’	value relative to rotating frame of reference

with these limitations being surmounted, this thermal cycle is reconsidered. For example, Dostal et al. [4] from MIT performed the investigation of the family of SCO_2 Brayton power cycles for application to next generation nuclear reactors. To identify potential technical risk items of the cycle, Sandia National Laboratory (SNL) [5] and many other institutions [6, 7] performed a series of experimental study and theoretical research of small-size SCO_2 cycle devices.

In order to take advantage of the attractive physical properties of SCO_2, the main compressors in a Brayton cycle are always working near the critical point as close as possible. Its performance has a direct impact on the thermal efficiency of the SCO_2 Brayton cycle. Nowadays, three-dimensional (3D) CFD are commonly adopted to analyze the flow in a centrifugal compressor. For the SCO_2 centrifugal compressors, many researchers Pecnik [8–11], Ameli [12], Hosangadi [13] conducted a series of three dimensional CFD simulations of a small-sized SCO_2 centrifugal compressor of SNL. They captured the CO_2’s state below the saturated line, which denotes the regions where condensation phase transformation appears most likely. They also investigated the aero-dynamic performance of the centrifugal compressor

through the CFD simulations. However, in some cases relatively large differences were found between predicttions and experimental measurements. Pecnik et al. attributed these errors to the simplified geometry adopted in the simulation. In addition, presently, the 3D CFD simulations for SCO_2 centrifugal compressors seem very hard to reach convergence, and always take a long time.

Generally, in the preliminary design stage, a 1D method is always adopted to quickly examine the aerodynamic performance of the centrifugal compressor. For traditional centrifugal compressors, there exists a sets of mean streamline analysis methods in the open literature, such as those published by Galvas [14], Aungier [15] and Oh et al. [16]. However, most of the loss prediction models were developed based on air, of which the properties are always far away from its critical point. Consequently, it should be verified to apply traditional loss models and empirical corrections in the analysis of SCO_2 compressors Moreover, accurate calculations of the SCO_2's physical properties during the analysis should also be concerned. To do this, a mean streamline analysis and design method was developed by Monge [17] for SCO_2 centrifugal compressors based on total pressure losses models. The predicted results were validated against the experimental data obtained from SNL. There exists a maximum error of 5.54% in the total pressure, indicating that this method had the potential for predicting the performance of the SCO_2 centrifugal compressors within acceptable error. By contrast, Lee et al. [18] adopted enthalpy-based loss models for designing and analysing SCO_2 turbomachines instead of total pressure loss models. The predicted results showed a similar tendency in pressure ratio compared to experimental data also acquired from SNL. However, some discrepancies were observed for the efficiencies. It is worth mentioning that in previous works related to the 1D analysis for SCO_2 centrifugal compressors, only single stage cases were investigated, and the agreements and discrepancies were not illustrated in detail as well. Moreover, a single stage compressor is insufficient to reach the cycle optimum pressure ratio especially when the compressors operate near the critical point of CO_2. As a result, multistage SCO_2 centrifugal compressors should be employed. Aimed at these objectives, it is crucial to ascertain the effectiveness of applying traditional losses models to predict the performance of multistage SCO_2 centrifugal compressors.

In this study, a 1D analysis method was developed to examine and evaluate the effectiveness of conventional loss models and empirical correlations for predicting performance of multistage SCO_2 centrifugal compressors. Both enthalpy-based loss models and total pressure loss models are adopted to evaluate the performance of the rotating and stationary components, respectively. To do this, the present paper starts with a review of conventional empirical correlations for enthalpy losses and total pressure losses in centrifugal compressors. Then the flow chart of the 1D method is described, and the experimental data from the single-stage SNL centrifugal compressor are used to validate the 1D method. Subsequently, the 1D analysis method is applied to analyze a two-stage SCO_2 centrifugal compressor. Due to the lack of relevant experimental data, 3D CFD simulations were carried out. Finally, detailed comparisons between the CFD and 1D prediction results are conducted. The features of the deviations are analyzed in detail, as well as the potential reasons that might cause these deviations.

2. Loss Model Categories

Accurate calculation of losses plays an important role in a correct performance prediction of centrifugal compressors using 1D analysis method. According to the ways accounting for flow losses, the loss models can be divided into two classes. One is referred as the enthalpy loss model or work loss model, and the other one is known as the total pressure loss model. The former model can determine the difference between the ideal enthalpy change and the actual enthalpy change, while the latter one can identify the deviation of the actual total pressure (relative total pressure for rotor) from the ideal total pressure. The actual enthalpy change is always bigger than the ideal one, but the actual total pressure loss is normally lower than the ideal value.

The two types of loss models can be distinguished by Eqs. (1) and (2), where f_c is a correction factor applied to the summation of all loss coefficients. For stationary components f_c=1; for impellers $f_c = \left(\rho'_{02}T'_{02}\right)/\left(\rho'_{01}T'_{01}\right)$.

$$h_{02} = h_{02,\text{ideal}} + \sum_{1\to 2} \Delta h_{\text{loss}} \tag{1}$$

$$P'_{02} = P'_{02,\text{ideal}} - f_c\left(P'_{01} - P_1\right)\sum_{1\to 2} \varpi_{\text{loss}} \tag{2}$$

In this study, the two loss definitions are both adopted in a hybrid way. The enthalpy loss models are used for predicting the performance of the impeller, while the total pressure loss models are employed for the stationary components in a centrifugal compressor, such as diffuser and return channel. Because when total enthalpy is constant, namely for stationary components, the total pressure loss models can work quite well. Aungier [26] pointed out that these models could correlate losses well over a wide range of Mach numbers. But for the impeller, total enthalpy is not constant, so additional care is required to account for the effect of the total enthalpy change on total pressure losses. To do this, Aungier [26]

applied the factor f_c mentioned above to correct the loss coefficients for impellers, however the factor was only applied to ideal gases. In addition, most models accounting for the losses in centrifugal impellers are based on enthalpy. Therefore, enthalpy loss models were used for predicting losses in impeller, instead of total pressure loss models.

According to the effect of the losses on the thermodynamic process, losses are commonly distinguished as internal losses and external losses, and the latter are also known as parasitic losses. The internal losses result from the irreversible compression process; they are the main reasons for the decrement of the total pressure, and exist both in the rotating and stationary parts. The parasitic losses account for the part of the extra mechanical work input which is not converted to total pressure rise. They only occur in rotating parts of a compressor. Internal losses used in the 1D analysis method include incidence loss, blade loading loss, skin friction loss, blade tip clearance loss, mixing loss and chocking loss. Parasitic losses considered here consist of disk friction loss, seal leakage loss and recirculation loss. All these loss models are described in the following section.

2.1 Loss models for impeller

2.1.1 Incidence loss

The incidence loss originates from the difference of the actual flow angle and the inlet blade angle. It always occurs in the region near the blade leading edge. Galvas [14], Aungier [15] and Conard [19] developed different correlations to determine this loss. Correlation adopted here is the one from Aungier [15].

$$\Delta h_{\mathrm{inc}} = 0.4\left(w_1 - c_{\mathrm{m1}}/\cos\beta_1\right)^2 \tag{3}$$

Eq. (3) should be applied at hub, mid-span and shroud with the weighting factors of 1/12, 10/12 and 1/12, respectively, as suggested by Aungier [15]. The final inlet incidence loss is defined as weighted average of the incidence losses at these three locations.

2.1.2 Blade loading loss

The blade loading loss occurs due to the pressure gradient in the impeller channel. The pressure gradient in the streamwise direction thickens the boundary layer, and pressure gradients in both spanwise and pitchwise result in the deflection of streamlines inside the impeller. This process induces the loss in momentum of the flow. Therefore, as described by Jansen [20], the blade loading loss is "the momentum loss due to boundary layer build-up". This loss is evaluated using the model proposed by Coppage et al. [21] as formulated in Eq. (4), where D_f is the diffusion factor which could be determined via Eq. (5).

$$\Delta h_{\mathrm{bl}} = 0.05 D_{\mathrm{f}}^2 u_2^2 \tag{4}$$

$$D_{\mathrm{f}} = 1 - \frac{w_2}{w_{1\mathrm{t}}} + \frac{\dfrac{0.75\Delta h_{\mathrm{Euler}}}{u_2^2}}{\left(\dfrac{w_{1\mathrm{t}}}{w_2}\right)\left[\left(\dfrac{Z}{\pi}\right)\left(1 - \dfrac{D_{1\mathrm{t}}}{D_2}\right) + \dfrac{2D_{1\mathrm{t}}}{D_2}\right]} \tag{5}$$

2.1.3 Skin friction loss

The skin friction loss accounts for the work done by the viscous shear forces in the flow boundary layer when the fluid flows over the channel surface. As suggested by Janson [20], the skin friction loss can be modelled as:

$$\Delta \mathrm{h}_{\mathrm{sf}} = 2c_{\mathrm{f}} \frac{L_{\mathrm{b}}}{d_{\mathrm{H}}} \overline{w}^2 \tag{6}$$

where the mean relative $\overline{w}$ can be calculated through:

$$\overline{w} = \frac{c_{1\mathrm{t}} + c_2 + w_{1\mathrm{t}} + 2w_{1\mathrm{h}} + 3w_2}{8} \tag{7}$$

2.1.4 Mixing loss

It is known that there is a jet-wake flow pattern at impeller outlet. When the wake flow mixes with the free stream flow, the mixing loss is generated. The mixing loss model improved by Johnston and Dean [22] on the basis of abrupt expansion losses is used here:

$$\Delta h_{\mathrm{mix}} = \frac{1}{1 + \tan^2\alpha_2}\left(\frac{1 - \varepsilon_{\mathrm{w}} - b_3/b_2}{1 - \varepsilon_{\mathrm{w}}}\right)^2 \frac{c_2^2}{2} \tag{8}$$

where ε_w is the wake fraction of the blade-to-blade space. The concept of diffusion factor given by Lieblein [23] can be used to estimate ε_w. Aungier [26] has generalized the diffusion factor to radial blades. More detailed calculation method can be found in Ref. [26].

2.1.5 Choking loss

With the increase of the mass flow, it is potential to approach sonic conditions at the impeller throat, which results in additional choking loss. When the sonic condition is reached, the model proposed by Aungier [15] is utilized for determining this choking loss:

$$\Delta h_{\mathrm{ch}} = \begin{cases} 0 & X \le 0 \\ 0.5 w_1^2 \left(0.05X + X^7\right) & X > 0 \end{cases} \tag{9}$$

where X is the judgment criterion for estimating whether the sonic condition is met. Its definition can be found in Ref. [15].

2.1.6 Blade tip clearance loss

The blade tip clearance loss only exists in open impellers. A portion of flow near blade tip flows through the gap between the blade tip and shroud, then it mixes with the main stream flow, causing the blade tip clearance loss. It can be modeled by the correlation given by Jansen [20]:

$$\Delta h_{\mathrm{cl}} = 0.6\frac{\varepsilon}{b_2}c_{\mathrm{u2}}\left\{\frac{4\pi}{b_2 Z}\left[\frac{r_{\mathrm{1t}}^2 - r_{\mathrm{1h}}^2}{\left(r_2 - r_{\mathrm{1t}}\right)\left(1+\frac{\rho_2}{\rho_1}\right)}\right]c_{\mathrm{u2}}c_{\mathrm{m1}}\right\}^{\frac{1}{2}} \quad (10)$$

where ε is the average size of the blade tip gap from inlet to outlet.

2.1.7 Disk friction loss

A cavity always exists between the impeller back surface and the surface of the stationary components, and such a cavity also exists over the impeller front surface for a closed impeller. The fluid flowing over the rotating disk surface introduces parasitic disk friction loss to the impeller. This loss is commonly calculated through the correlation derived by Daily and Nece [24] based on their smooth plane disk experiments:

$$\Delta h_{\mathrm{df}} = C_{\mathrm{fdf}}\frac{\overline{\rho} d_2^2 u_2^3}{16\dot{m}} \quad (11)$$

2.1.8 Recirculation loss

When a centrifugal compressor operates at off-design conditions, in particular at lower flow conditions than the design point, a portion of flow is likely to flow back to the impeller due to the high flow diffusion at these conditions. This will lead to an increase in impeller work input which is termed as recirculation loss. In this paper, the recirculation loss is determined through the model given by Oh et al. [16].

$$\Delta h_{\mathrm{rc}} = 8\times10^{-5}\sin h\left(3.5\alpha_2^3\right)D_{\mathrm{f}}^2 u_2^2 \quad (12)$$

The calculation of the diffusion factor D_{f} here is the same as that in blade loading loss, and the impeller outlet flow angle α_2 is in radian.

2.1.9 Seal leakage loss

A certain leakage flow through seals leads to seal leakage loss, reducing the effective mass flow. This loss can be estimated by the correlation given by Aungier [15]

$$\Delta h_{\mathrm{lk}} = \frac{\dot{m}_{\mathrm{cl}} u_{\mathrm{cl}} u_2}{2\dot{m}} \quad (13)$$

2.1.10 Slip factor

The fluid entering the impeller cannot be guided perfectly due to the finite number of blades, resulting in a deviation angle from the blade metal angle. It is necessary to accurately predict the flow deviation angle in 1D modeling because the work input of the impeller blade directly depends on the exit angle and so does the pressure rise. In this study, the slip factor model developed by Qiu et al. [25] is adopted,

$$\sigma = 1 - \frac{c_{\mathrm{slip}}}{u_2} = 1 - \frac{F\pi\cos\beta_{\mathrm{2b}}\sin\gamma_2}{Z_2} - \frac{Fs_2\phi_2}{4\cos\beta_{\mathrm{2b}}}\left(\frac{\mathrm{d}\beta}{\mathrm{d}m}\right)_2 \quad (14)$$

where F is the shape factor and s_2 is the pitch at blade outlet.

2.2 Loss models for diffuser and return channel

Different from loss models for impeller, all loss models for predicting flow parameters in stationary components are based on total pressure loss. The relevant correlations to evaluate the losses in the vaned diffuser and return channel vane are listed in Table 1 and Table 2, respectively. Those models are presented by Aungier [26].

Vaneless zones always exist in a centrifugal compressor regardless of whether it is single stage or multistage. For multistage cases, there are usually three vaneless zones in a middle stage with vaned diffuser (two for stages with vaneless diffuser). One is present between impeller outlet and vaned diffuser inlet; another one locates between diffuser outlet and return channel inlet, which is known as crossover bend; the last one is the zone following the return channel vanes. The approach

Table 1 Loss models for vaned diffuser [26]

Loss classification	Loss coefficient correlation
Incidence loss	$\varpi_{\mathrm{inc,DIF}} = \begin{cases} \varpi_{\mathrm{inc0,DIF}} + 0.8\left(\dfrac{c_3 - c_3^*}{c_3}\right)^2 & c_3 \le c_{3\mathrm{s}} \\ \varpi_{\mathrm{inc0,DIF}} + 0.8\left\{\left[\left(\dfrac{c_3}{c_{3\mathrm{s}}}\right)^2 - 1\right]\left(\dfrac{c_{\mathrm{th,DIF}}}{c_3}\right)^2 + \left(\dfrac{c_{3\mathrm{s}} - c_3^*}{c_{3\mathrm{s}}}\right)^2\right\} & c_3 > c_{3\mathrm{s}} \end{cases}$ $\varpi_{\mathrm{inc0,DIF}} = 0.8\left(\dfrac{c_3^* - c_{\mathrm{th}}}{c_3}\right)^2 + \left(\dfrac{z_{\mathrm{DIF}} t_3}{2\pi r_3}\right)^2;\ c_3^* = \dfrac{c_{3\mathrm{m}}}{\cos\alpha^*} = \dfrac{c_{3\mathrm{m}}}{\sqrt{\cos\beta_3\cos\alpha_{\mathrm{th}}}}$
Skin friction loss	$\varpi_{\mathrm{fr,DIF}} = 4c_{\mathrm{f}}\dfrac{L_{\mathrm{B,DIF}}}{d_{\mathrm{H,DIF}}}\left(\dfrac{\overline{c}}{c_3}\right)^2\left(\dfrac{\overline{d}_{\mathrm{H,DIF}}}{2\delta}\right)^{0.25}$
Mixing loss	$\varpi_{\mathrm{mix,DIF}} = \left(\dfrac{c_{\mathrm{m4,wake}} - c_{\mathrm{m4,mix}}}{c_3}\right)^2$

Table 2 Loss models for return channel vane [26]

Loss classification	Loss coefficient correlation
Incidence loss	$\varpi_{\text{inc,RC}} = 0.8\left(1-\frac{c_{\text{m6}}}{c_6 \sin\alpha^*}\right)^2$
Skin friction loss	$\varpi_{\text{sf,RC}} = 4c_{\text{f}}\left(\frac{\bar{c}}{c_6}\right)^2 \frac{L_{\text{B}}}{d_{\text{H}}} + \frac{c_{\text{m6}}c_{\text{m7}}\lvert\alpha_{c6}-\alpha_{c7}\rvert}{13c_6^2}$
Blade loading loss	$\varpi_{\text{bl,RC}} = \frac{2\pi^2}{3}\left(\frac{r_6c_{\text{u6}}-r_7c_{\text{u7}}}{z_{\text{RC}}L_{\text{B}}c_6}\right)^2$
Mixing loss	$\varpi_{\text{mix,RC}} = \left(\frac{c_{\text{m,wake}}-c_{\text{m,mix}}}{c_6}\right)^2$

used here to estimate the fluid thermal states in such vaneless zones is based on a differential form of conservation laws employed by Aungier [26]. This model accounts for the losses arising from friction, diffusion and streamline curvature. Relevant correlations involved in this model are shown as following:

$$\dot{m} = 2\pi rb(1-B)\rho c_{\text{m}} \qquad bc_{\text{m}}\frac{\text{d}(rc_{\text{u}})}{\text{d}m} = -rcc_{\text{u}}c_{\text{f}}$$

$$\frac{1}{\rho}\frac{\text{d}p}{\text{d}m} = \frac{c_{\text{u}}^2\sin\alpha_{\text{c}}}{r} - c_{\text{m}}\frac{\text{d}c_{\text{m}}}{\text{d}m} - \frac{cc_{\text{m}}c_{\text{f}}}{b} - \frac{\text{d}I_{\text{D}}}{\text{d}m} - I_{\text{c}} \qquad (15)$$

$$h_0 = h + \frac{1}{2}c^2$$

3. 1D Analysis Method for Multistage SCO_2 Centrifugal Compressors

Based on the empirical loss formulations summarized above, a 1D method to predict the aerodynamic performance of multistage SCO_2 centrifugal compressors is developed. Figure 1 shows the flow diagram for conducting the 1D performance analysis. Eight stations for each middle stage are specified for modeling purpose. They are indexed by 1 to 8 as shown in Fig. 2, corresponding to impeller inlet and outlet, vaned diffuser inlet and outlet, crossover bend inlet, return channel vane inlet and outlet, and stage outlet, respectively. It should be noted that when the stage has a vaneless diffuser only, stations 3 to 5 are the same station.

As mentioned in the introduction part, tiny changes of pressure and temperature can cause strong variation of the physical properties of CO_2 near the critical point. To consider the real gas effects, the equation of state (EOS) model developed by Span and Wagner [27] was adopted in this study, since it has been regarded as the most accurate EOS model for carbon dioxide. The relevant subroutines in REFPROP [28] developed by NIST are called during the 1D analysis to determine the thermal states.

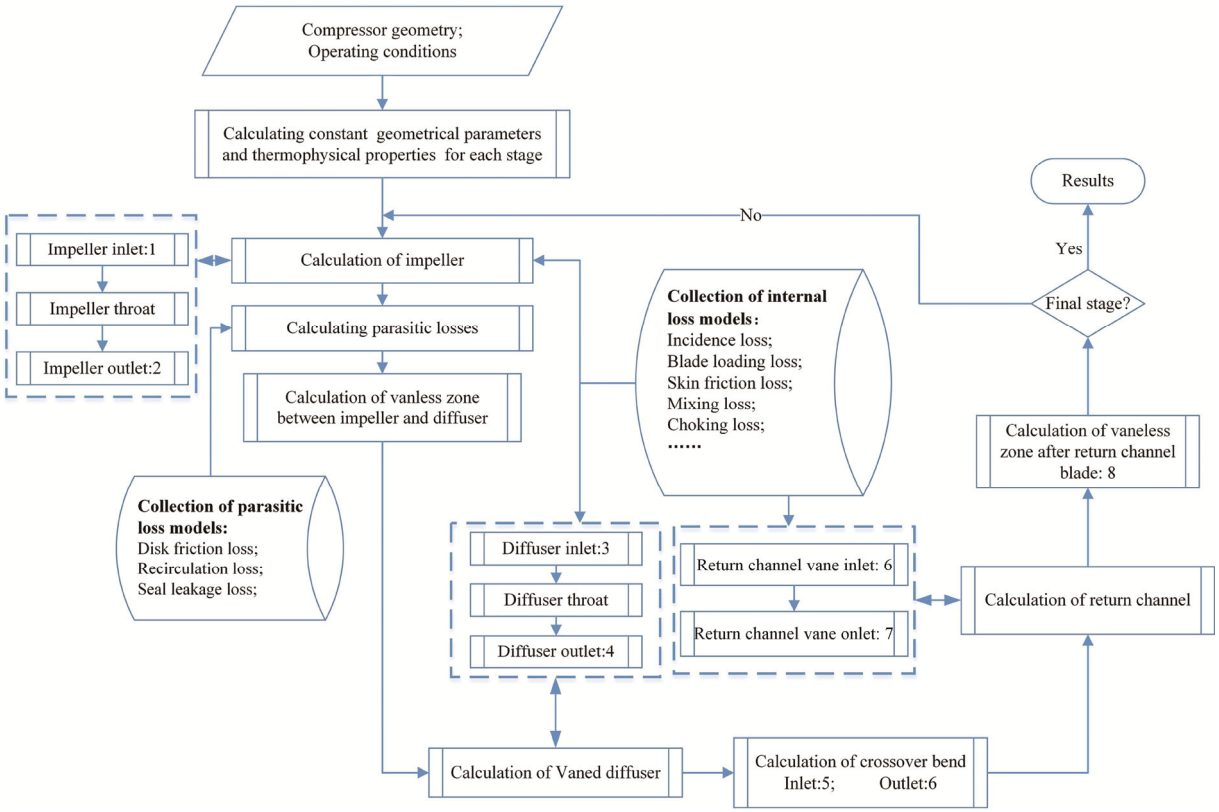

Fig. 1 Flow diagram for the 1D performance prediction of multistage centrifugal compressors

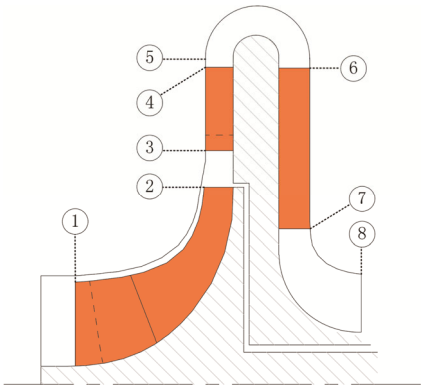

Fig. 2 Computational stations in one stage of a multistage centrifugal compressor

4. Validation for a Single Stage SCO_2 Centrifugal Compressor

The 1D analysis method developed in this study is firstly validated against the experimental results of a single stage SCO_2 centrifugal compressor with vaned diffuser tested by SNL. This compressor was tested near the critical point (T_c=304.2 K, P_c=7.4 MPa). As can be seen from table 3, the inlet temperature ranges from 305.5 K to 308.7 K, and the inlet pressure varies from 7.68 MPa to 8.29 MPa. All the geometrical information of the impeller can be found in Ref. [5], and additional vaned diffuser data can be found in Ref. [17].

Monge [12] extracted and organized part of the experimental results of the SCO_2 centrifugal compressor tested by SNL, and listed them in a table form. These points at different operating conditions are also used in this study to validate the 1D analysis method. Table 3 presents the experimental and 1D computational results.

In Table 3, N is the rotating speed; T_{00} and P_{00} stand for the total temperature and the total pressure at impeller inlet, respectively; Q_m is the mass flow rate; P_2 and P_{04} correspond, respectively, to the static pressure at impeller outlet and the total pressure at diffuser outlet. As observed from Table 3, the average deviation of the static pressure at impeller outlet is 1.2%, and the maximum deviation is 3.6%, occurring at a relatively high rotating speed. With respect to the total pressure at diffuser outlet, the mean deviation is −0.4%, and maximum deviation is −5.5%, also occurring at a relatively high rotating speed of 56 000 r/min. With decreasing the rotating speed, the deviations also decrease.

In order to validate the capability of the loss models in predicting the efficiency of a single stage SCO_2 centrifugal compressor, the experimental data of the SNL's SCO_2 centrifugal compressor operating at 55 000 r/min are employed. The performance curves predicted by the present 1D method, the one developed by Aungier [26], and the one developed by Lee et al. [18] from KAIST, and the experimental performance data are compared in Fig. 3. Compared with the present 1D method, the 1D method developed by Aungier was fully based on pressure loss models, and only enthalpy loss models were adopted in the KAIST's 1D method to analyze the SCO_2 compressor. The pressure loss models for the impeller developed by Aungier are summarized in Table 4. The KAIST's 1D method adopted the same set of enthalpy loss models for the impeller as the present one, except for the incidence loss [18].

Table 3 Comparison of experimental and 1D analytical results

N/ r·min^{-1}	T_{00}/ K	P_{00}/ MPa	Q_m/ kg·s^{-1}	$P_{2\text{-}1D}$/ MPa	$P_{2\text{-}Exp}$/ MPa	Dev	$P_{04\text{-}1D}$/ MPa	$P_{04\text{-}Exp}$/ MPa	Dev
10 000	305.5	7.68	0.454	7.74	7.68	0.8%	7.77	7.98	−2.6%
20 000	305.5	7.68	0.771	7.94	7.85	1.1%	8.09	8.07	0.2%
28 000	305.5	7.68	1.134	8.19	8.21	−0.3%	8.48	8.53	−0.7%
39 000	305.6	7.71	1.451	8.77	8.57	2.3%	9.356	9.28	0.8%
49 000	306.3	7.85	1.816	9.53	9.43	1.1%	10.47	10.64	−1.6%
55 000	306.4	7.89	2.043	10.05	10.00	0.5%	11.26	11.35	−0.8%
56 000	306.6	7.83	2.088	9.75	10.10	−3.5%	10.87	11.50	−5.5%
60 000	306.9	8.00	2.225	10.58	10.21	3.6%	12.04	12.14	−0.9%
64 900	307.9	8.21	2.406	11.23	10.85	3.5%	12.95	12.92	0.2%
64 384	308.7	8.29	2.860	10.86	10.67	1.8%	12.39	11.94	3.7%
29 888	306.7	7.92	1.315	8.46	8.26	2.4%	8.77	8.57	2.4%
		Minimum deviation				−0.3%			0.2%
		Maximum deviation				3.6%			−5.5%
		Average deviation				1.2%			−0.4%

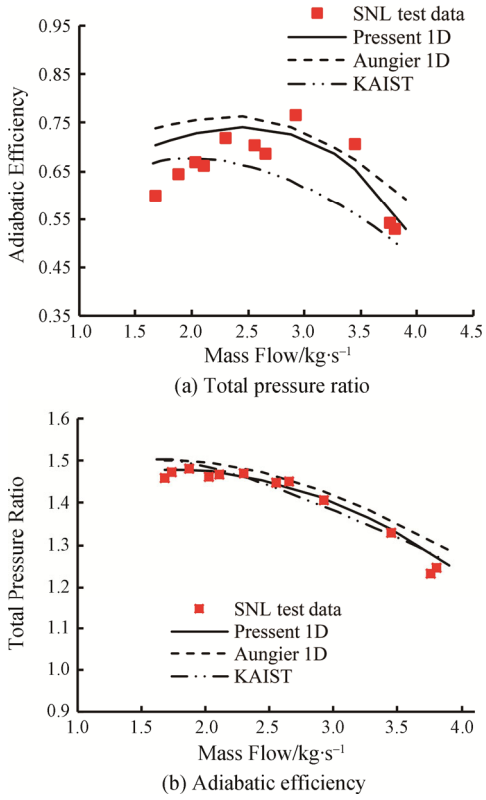

Fig. 3 Comparison of 1D predicted and experimental performance data of the SCO_2 single stage compressor from SNL

Table 4 Pressure loss models for impeller developed by Aungier [26]

Loss classification	Loss coefficient correlation
Incidence loss	$\varpi_{inc}=0.8\left(1-\frac{c_{m1}}{w_1\cos\beta_1}\right)^2+\left(\frac{z_{FB}l_1}{2\pi r_1\cos\beta_1}\right)^2$
Inlet diffusion loss	$\varpi_{diff}=0.8\left(1-\frac{w_{th}}{w_1}\right)^2-\varpi_{inc}$ $\quad \varpi_{diff}\geq 0$
	$\varpi_{diff}\geq\left(\frac{w_{1s}-1.75w_{th}}{w_1}\right)^2-\varpi_{inc}$ $\quad \frac{w_{1s}}{w_{th}}\geq 1.75$
Blade loading loss	$\varpi_{bl}=\frac{1}{24}\left(\frac{\Delta w}{w_1}\right)^2+\frac{1}{6}\left(\frac{\bar{k}_m\bar{b}\bar{w}}{w_1}\right)^2$
Skin friction loss	$\varpi_{sf}=4c_f\frac{L_B}{\bar{d}_H}\left(\frac{\bar{w}}{w_1}\right)^2$
Clearance loss	$\varpi_{cl}=\frac{2\dot{m}_{cl}\Delta P_{cl}}{\dot{m}\rho_1 w_1^2}$
Mixing loss	$\varpi_{mix}=\left[\frac{(\lambda-1)c_{m2}}{w_1}\right]^2$

It can be seen that a better agreement with the experimental data is obtained by the present 1D method both for the adiabatic ratio and the pressure ratio. However, all the methods predicted slightly higher pressure ratios than the experimental value at the maximum flow rate. As for the adiabatic efficiency, the results obtained by the present 1D method match the experimental data well when the mass flow rate is higher than 2.3 kg/s. On the contrary, the Aungier's 1D method predicted a much flatter efficiency curve, and the KAIST's 1D method predicted a much lower one when the mass flow rate is higher than 2.3 kg/s. For the mass flow lower than 2.3 kg/s, relatively large deviations from the experimental data are observed for the efficiency curves predicted by the three methods, which reveals the deficiencies of the 1D loss models in predicting the efficiency of a single stage SCO_2 centrifugal compressor working at low flow rate.

5. Evaluation for a Two-Stage SCO_2 Centrifugal Compressor

A single stage compressor such as the one at SNL is insufficient to reach the optimum pressure ratio in a large power system, while achieving a high cycle efficiency and reducing the possibility of fluid condensation at impeller inlet. Monge [17] presented a three-stage centrifugal compressor design for the compression system of a 10 MW power plant. In the present study, the first two stages of that three-stage centrifugal compressor were designed based on the main dimensions of the impeller and the design specifications which are available in Ref. [17]. Then the two-stage centrifugal compressor was used to evaluate the 1D conventional loss models.

The total inlet temperature and pressure of the compressor are 313 K and 7.5 MPa, respectively, which are also slightly above the critical point. The design mass flow is 73.04 kg/s, and the rotating speed is 15 184 r/min as presented in Ref. [17]. The first stage consists of an impeller with 20 full blades and 20 splitter blades, a vaneless diffuser and a return channel with 15 vanes. The second stage also comprises an impeller with 20 full blades and 20 splitter blades and a vaneless diffuser. Fig. 4 and Table 5 present a sketch and design details of the two stages.

5.1 Three-dimensional CFD simulation

Three-dimensional CFD simulations were performed, due to lacking experimental data. The CFD simulations were performed by the commercial solver NUMECA FINE^{TM}/Turbo. To reduce time costs, the computational domain only contains one single passage, which includes one splitter and one main blade for each impeller. For the inlet boundary, the total temperature and total pressure were imposed, and the outlet boundary condition was specified by an average static pressure.

Although the Span-Wagner EOS model [27] is accurate, it is computationally expensive. Therefore, a

Fig. 4 First two stages geometry of a three-stage SCO_2 centrifugal compressor

Table 5 Design details of the two stages

Stage number	1	2
Design total pressure ratio	1.55	1.53
Specific speed	0.69	0.54
Specific diameter	3.38	4.22
Impeller		
Inlet shroud radius/mm	53.1	49.46
Inlet hub radius/mm	25.0	25.0
Inlet blade angle at shroud	−58.8°	−59°
Inlet blade angle at hub	−40.6°	−43°
Exit radius/mm	86.74	92
Exit blade height/mm	7.72	6.42
Exit blade angle	−1.5°	−1.5°
Number of full blades	20	20
Number of splitter blades	20	20
Leading edge thickness/mm	1	1
Trailing edge thickness/mm	1	1
Tip clearance/mm	0.12	0.12
Axial length/mm	55.0	54.8
Vaneless diffuser		
Inlet radius/mm	86.74	92
Inlet width/mm	7.84	6.54
Exit radius/mm	160.56	148
Exit width/mm	6.6	4.9
Return channel		
Hub curvature radius of crossover/mm	7.84	-
Inlet radius/mm	160.47	-
Inlet blade height/mm	9.08	-
Radius at trailing edge/mm	80.24	-
Blade height at trailing edge/mm	10.0	-
Average exit radius/mm	37.23	-
Exit width/mm	24.46	-

fast and stable interpolation method based on look-up property tables was adopted to determine the fluid states during the CFD simulation. All the property tables were generated through the TABGEN module of NUMECA software.

The k-ε turbulence model with wall functions was used to simulate the turbulence effects in the compressor. The unique physical properties of SCO_2 result in a very large Reynolds number in the multistage compressor. If low Reynolds number turbulence models were used to simulate the flow, y^+ values should be adjusted close to unity and the size of the first grid layer would be in the order of 10^{-8} m [17]. This may be feasible for the Sandia small scale single stage compressor, but for the much larger multistage compressor this will result in a very large number of grid nodes to obtain reasonable grid quality, which is beyond the computational capacity of the authors. Therefore, the high Reynolds k-ε turbulence model was used in this study. The height of the first layer of the grids was set to 0.001 mm to ensure that y^+ values were distributed between 20 and 50. Since one row of splitter blade was included in the impeller, the H&I mesh topology was used to obtain better mesh quality. The near design operating point was selected to examine the grid sensitivity. Figure 5 displays the variations of the mass flow rate and the adiabatic efficiency as a function of the grid node numbers. According to the results of the grid sensitivity study, the third set of grid with 2.2 million nodes was selected for the subsequent CFD simulations.

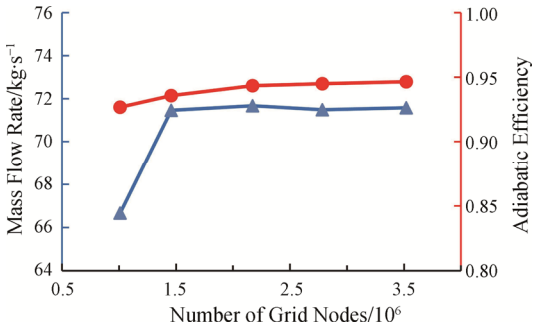

Fig. 5 Results of grid sensitivity study

5.2 3D CFD and 1D prediction results

The performance curves calculated by the 1D method and 3D CFD simulations are compared in Fig. 6. It should be noted that impeller backside cavities and seals were not included in the geometrical model for the CFD simulations. Hence, the parasitic losses calculated by the 1D method were not included for comparison in this section.

It could be observed that the 1D results showed similar performance trends with the CFD results in general. For both the pressure ratio and the adiabatic efficiency, the differences increase with decreasing the

flow rate. The differences reach maximum at the lowest mass flow, where the pressure ratio predicted by the 1D method is 5.6% lower than that predicted by CFD, and the adiabatic efficiency is 6.4% lower. In addition, due to the nearly radial exit blade angels (−1.5°) of the two impellers, the total pressure curves turn out flat for both methods. The pressure curve predicted by the 1D method is found to be much flatter than the CFD predicted. However, it is hard to conclude which method is more accurate without experimental verification, and many relevant researches [9, 11] suggested that the pressure ratio and stage efficiency predicted by CFD simulations were higher than experimental data.

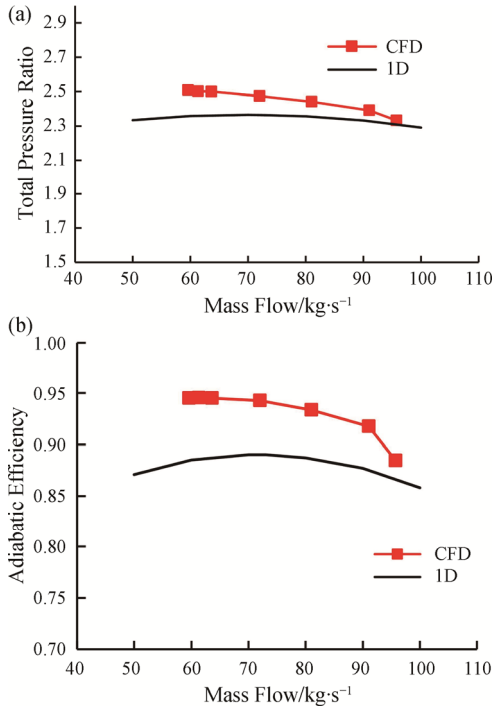

Fig. 6 Comparison of performance curves predicted by 1D method and CFD simulations

In order to figure out the reasons for the differences in the performance results predicted by the two methods, also given the geometrical similarities of the two stages, more performance parameters were extracted and compared for the first stage in this study. It is known that the pressure ratio generated by a compressor mainly depends on the aerodynamic efficiency and the blade work coefficient, which also interact with each other in a real compression process. In this study, no prewhirl was assumed, then the blade work coefficient could be expressed by

$$I_{\text{blade}} = \frac{c_{\text{u2}}}{u_2} = \left(1 - \frac{1-\sigma}{1+\phi_2 \tan\beta_{2\text{b}}}\right) \times \left(1 + \frac{1}{1-B_2}\frac{\dot{m}}{\rho_2 A_2 u_2}\tan\beta_{2\text{b}}\right) \tag{16}$$

where the slip factor σ adopted here is the one proposed by Qiu et al. [18] and it maintains constant when dβ/dm is zero.

Fig. 7 shows the comparison of c_{u2}/u_2 calculated by CFD and 1D method. Both curves have similar flat trend, but the blade work coefficient calculated by the 1D method is found to be smaller than the CFD predicted value over the whole flow range. This can be explained through Fig. 8 and Fig. 9. The flow angles calculated by CFD and the 1D method are compared in Fig. 9. It could be observed that both the relative and absolute flow angles calculated by the 1D method at the same flow rates are smaller than those calculated by the CFD. These smaller angles obtained by the 1D method can finally result in smaller c_{u2}, which can be further demonstrated with Fig. 8. In this figure, the impeller exit velocity triangles calculated by the two methods at 73 kg/s are plotted. The relative velocity calculated by 1D method is found to be more tangential than the one calculated by CFD, denoting that the slip factor (σ=1–c_{slip}/u_2) modelled in the 1D method is relatively small. In addition, it can be also found in Fig. 8 that the impeller outlet flow coefficient (ϕ_2=c_{m2}/u_2) calculated by 1D method is bigger than the one calculated by CFD, which can further decrease the blade work coefficient. However, due to the nearly radial exit blade angles of the two impellers (−1.5°), tan$\beta_{2\text{b}}$ turns out close to zero. In addition, dβ/dm at impeller outlet is adjusted to zero during the design. Hence, according to Eqs. (17) and (18), it is the slip factor that dominates the blade work coefficient.

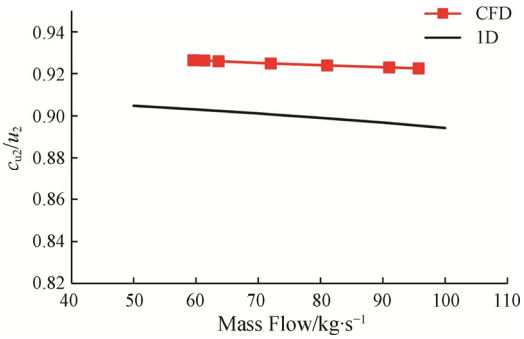

Fig. 7 Comparison of c_{u2}/u_2 at impeller outlet calculated by CFD and 1D method

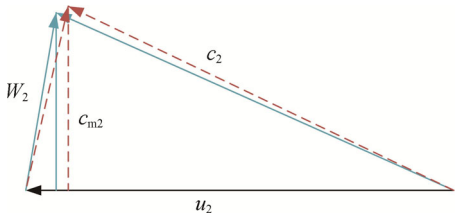

Fig. 8 Comparison of velocity triangles calculated by CFD (solid line) and 1D method (dashed line)

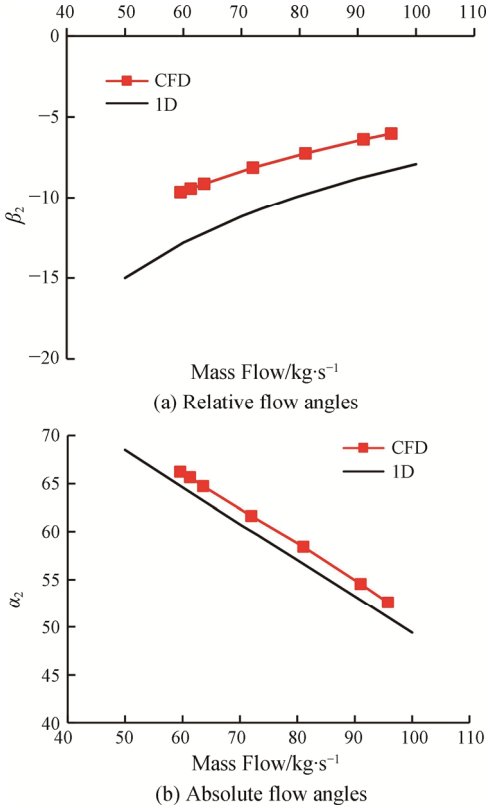

Fig. 9 Comparison of flow angles at impeller outlet calculated by CFD and 1D method

Therefore, it could be concluded that the underestimation of the slip factor in the 1D method is one of the reasons why the CFD predicted pressure ratio is higher than the 1D model.

$$\frac{\partial I_{\text{blade}}}{\partial \phi_2} = \tan \beta_{2\text{b}} - \frac{Fs_2}{4\cos \beta_{2\text{b}}}\left(\frac{\mathrm{d}\beta}{\mathrm{d}m}\right)_2 = \tan \beta_{2\text{b}} \tag{17}$$

$$\frac{\partial I_{\text{blade}}}{\partial \sigma} = 1 \tag{18}$$

In addition to the slip factor, another reason for the pressure ratio differences can be found from the different aerodynamic efficiencies predicted by the two methods, as shown in Fig. 10. Adiabatic efficiency and total pressure ratio predicted by CFD and 1D model at different stations in the first stage were compared in Fig. 10. The adiabatic efficiency at different stations is defined as

$$\eta_i = \frac{h_{0is} - h_{01}}{h_{0i} - h_{01}} \tag{19}$$

where the subscript 'i' represents different stations of interest in the stage.

The station positions are illustrated in Fig. 2. It can be observed that the efficiency and pressure ratio curves predicted by the two methods have similar performance trend when the mass flow rate is between 70 kg/s and 95 kg/s. But, when the mass flow is lower than 70 kg/s, the efficiency and pressure ratio predicted by the 1D method declines slightly with decreasing mass flow, however the results calculated through CFD almost keep constant.

The efficiencies are directly associated with the losses. High efficiency drop always relates to high loss, and vice versa. For the predictions of the CFD, it can be found that the losses occurring in the vaneless diffuser are the highest among all the components when the mass flow is lower than 82 kg/s. The losses occurring in return channel (from station 4 to station 8) maintain nearly constant over the whole operation range, except that the proportion of losses in the crossover increases slightly with increasing mass flow. When the mass flow is more than 81 kg/s, there is an evident decline in the efficiency, and a similar decrease is also expected in the pressure ratio. For the results predicted by 1D models, however, the losses occurring in the impeller take up the same percentage as the losses in the diffuser. Moreover, the 1D predictions show that the losses in the vaned zone of the return channel (from station 6 to station 7) increase with increasing mass flow, but those losses predicted by CFD are nearly constant. The losses occurring in the vaneless region between station 7 and station 8 are relatively smaller compared with the CFD predictions.

An additional insight into the distribution of the losses occurring in the impeller and the return channel vane can be beneficial in assessing performance predictions obtained with the 1D method. Non-dimensional enthalpy loss coefficient and total pressure loss coefficient were used to this objective. The former one is defined as Eq. (20), and is used to address the losses in the impeller. The total pressure loss coefficients have been presented in Table 2. They are used for the losses in the vaned zone of the return channel. For the 1D method, the loss components can be determined through the corresponding loss models as mentioned in the loss model categories section. However, the flow within the centrifugal compressor is highly complex, and all the losses interweave and interact with each other, making it difficult to predict loss components separately through CFD method. In this study, instead of analysing individual losses, losses in the impeller and return channel were divided into two parts for the CFD results. The first part was the region from the blade leading edge to the throat, and the second part was the region from the throat to the trailing edge. In addition, the method of extracting losses from CFD results for different regions in the impeller was based on Eq. (21), since it is easier and more convenient to be implemented than Eq. (1) in dealing with CFD results. In Fig. 11, total enthalpy loss coefficients at the impeller outlet calculated by those two different methods (Eq. (1) and Eq. (21)) are compared. It can be observed that the loss coefficients calculated

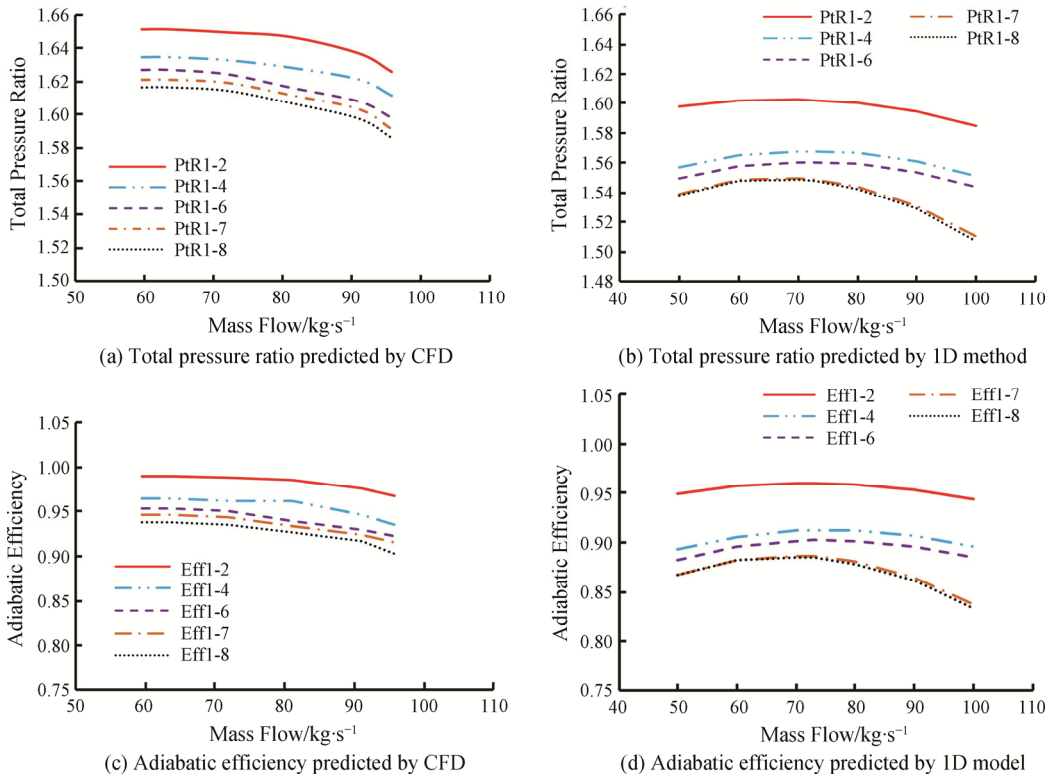

Fig. 10 Comparison of predictions of efficiency and pressure ratio provided by CFD and 1D method at different stations in the first stage

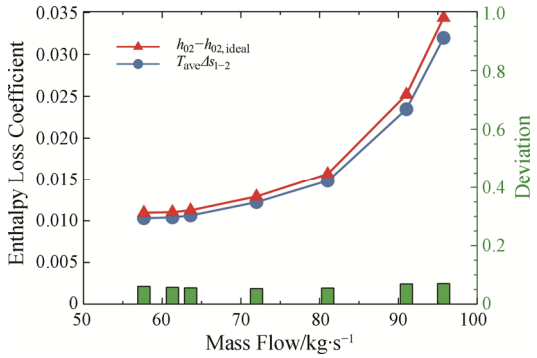

Fig. 11 Comparison of the total enthalpy loss coefficient at the impeller outlet calculated by two different methods

based on Eq. (21) are slightly lower than that using Eq. (1), and the farther the point away from the design point, the larger the deviation between the two results. The deviations mainly result from the following two reasons. The first and the most dominant reason is that Eq. (21) only accounts for the heat irreversibly transforming from mechanical energy, but Eq. (1) consists of both the irreversible losses and the extra compression work known as the heat resistance loss. The other reason is the way of calculating the average static temperature in Eq. (21) where a linear thermodynamic process is assumed. Given the fact that what matters is the proportion of the losses at different regions in the subsequent qualitative analysis, rather than the specific values of them, so adopting Eq. (21) is reasonable to extract enthalpy losses from the CFD results,

$$\xi = \frac{\Delta h_{\text{loss}}}{u_2^2} \tag{20}$$

where Δh_{loss} stands for different internal losses mentioned in the section of Loss Models for Impeller,

$$\Delta h_{\text{loss}} = T_{\text{ave}} \Delta s \tag{21}$$

where T_{ave} is the average static temperature of a thermodynamic process, and in this study T_{ave} is defined as $\frac{T_{\text{in}} + T_{\text{out}}}{2}$; Δs is the entropy increment from the inlet to the outlet of a region of interest.

The loss breakdown is shown in Fig. 12. For the losses in impeller calculated by 1D models, the skin friction loss seems to account for a particularly pronounced proportion in the whole flow range. It increases with the increase of the flow rate. On the contrary, the blade loading loss decreases with increasing the flow rate. The incidence loss increases as the operating condition deviates from the design point. At low flow rate, the skin friction loss, blade loading loss and incidence loss appear to have equal importance. Instead of individual losses, losses in impeller calculated by CFD method are divided

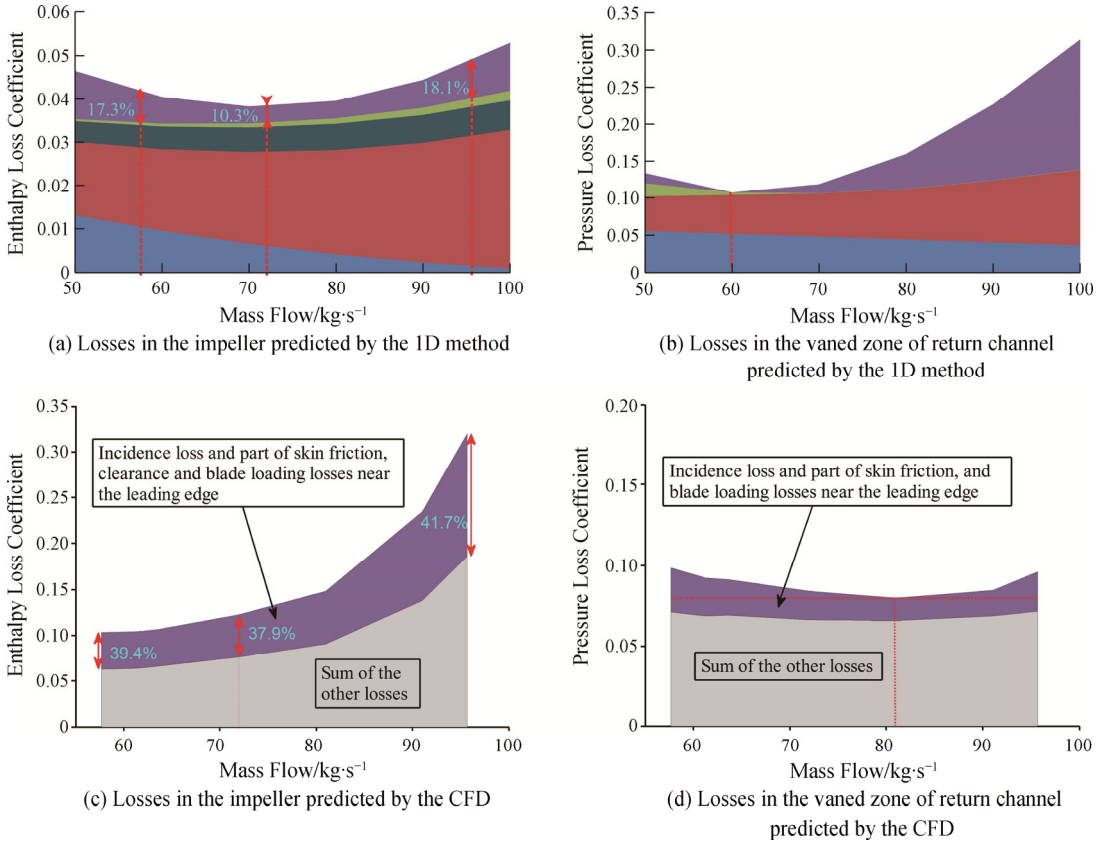

Fig. 12 Loss breakdown for the impeller and the return channel of the first stage

into two parts as shown in Fig. 12(c). The results show that the losses upstream the impeller throat also account for a large proportion. It can be inferred that this part of losses is mainly composed of incidence loss and only a few of other losses, because the blade surface area between the leading edge and the throat is only 6.05% of the whole blade surface area (including the splitter blade). Similarly, with the incidence loss predicted by the 1D method, the percentage of this part of losses also reaches the minimum near the design point, but its actual value maintains nearly constant at flow rate lower than the design value. The other losses between the throat and the trailing edge change relatively substantially over the whole flow range, in comparison to the 1D results, and this part of losses increases with the flow rate monotonically. Therefore, according to the characteristics of the losses predicted by the 1D models and the CFD, the 1D incidence loss model may predict much lower losses than the CFD, and the skin friction loss model and blade loading loss model may predict higher losses, especially at flow rate lower than the design value. This may be the main reason why the pressure ratio curve predicted by CFD is steeper compared with 1D predicted results at low flow rate as shown in Fig. 10.

For the vaned zone of the return channel, the incidence loss increases dramatically when the flow rate exceeds 73.04 kg/s. Because, for the return channel vane, the smallest incidence loss occurs at around 60 kg/s with an incidence angle of 3.7°, indicating that the optimum flow inlet angle (α^* in Table 2) for the return channel is 68°. Therefore, zero-incidence angle at the design mass flow does not correspond to zero incidence loss. When the mass flow exceeds the design mass flow, the incidence loss turns to be even higher due to the much larger deviation from the optimum incidence angle. It can be observed clearly that the incidence loss accounts for a very large proportion at high flow rate, causing large decline of the efficiency and the pressure ratio. The sum of the other losses keeps almost constant over the whole flow range. For the CFD results, the losses were also separated into two parts in this zone, like the way of dealing with the losses in the impeller. In Fig. 12(d), the losses downstream the throat are nearly constant, which is similar with the 1D results. However, the minimum value of the losses upstream the throat occurs at 81 kg/s, which is larger than the 1D result. This may be caused by the differences of the flow angles or the optimum flow inlet angle calculated by these two methods, since the incidence angle has a direct effect on the incidence loss. In Fig. 13, the absolute flow angles predicted by the two methods at the return channel vane inlet are compared and found to be in relatively good agreement, so the

effect of the flow angles could be ruled out. Therefore, it could be concluded that it may be the optimum flow inlet angle in the 1D incidence loss model presented in Table 2 that causes this deviation.

In addition, as can be seen in Fig. 10, the pressure ratio curve predicted by CFD for the impeller (i.e. PtR1-2) has a relatively large drop near the maximum flow rate. The losses between the leading edge and the throat in the impeller also increase obviously near the maximum flow rate. Usually this is mainly caused by the increase of the Mach number, resulting in the increase of the incidence

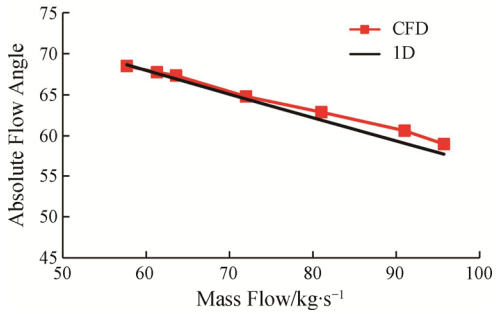

Fig. 13 Comparison of flow angles at return channel vane inlet calculated by the CFD and 1D method

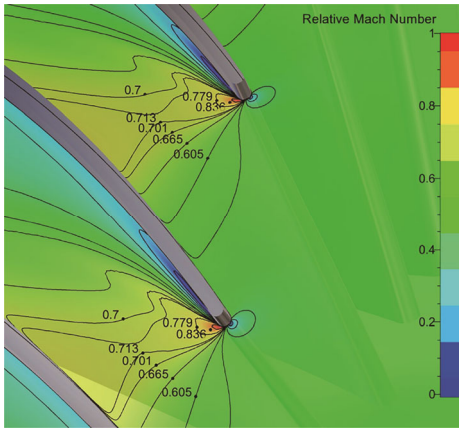

Fig. 14 Relative Mach number contour at 95% span position near the leading edge

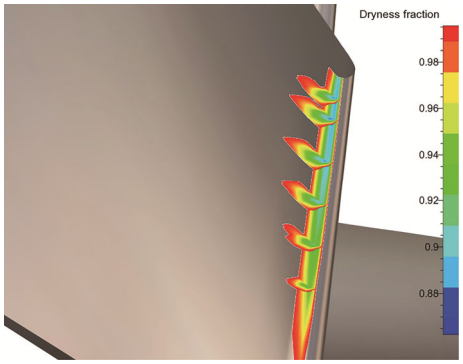

Fig. 15 The region where the dryness fraction is less than 1 near the leading edge

loss, skin friction loss, and choking loss in particular when sonic condition is reached at the impeller throat. As expected, an area of relatively large Mach number starts to grow near the leading edge as shown in Fig. 14. In addition, a unique phenomenon in the SCO_2 compressor working near the critical point has been captured as shown in Fig. 15 that a region where the dryness fraction of the fluid is less than 1 is found on the pressure surface near the leading edge, suggesting that fluid condensation may take place there, because this is also a region with relatively low temperature and low pressure due to local flow acceleration near the blade leading edge. When the decrease of temperature and pressure exceeds a certain value with increasing mass flow, thermodynamic properties may fall into the two-phase region below the saturation curve since the total inlet temperature and pressure are just slightly above the critical point. Then condensation can potentially occur, yielding formation of liquid droplets. Actually, the formation of liquid droplets does not only depend on the fluid state but also on the residence time. The fluid state determines the time needed for stable liquid droplets to form, namely, the nucleation time. If the residence time is smaller than the nucleation time, no liquid droplets will form even if the thermodynamic state of the fluid lies in two-phase zone. If the residence time is larger than the nucleation time, liquid droplets will form. The nonequilibrium and irreversible phase change and the mixing of liquid droplets with main flow will introduce additional losses which cannot be accounted for in the current 1D loss models. In this case the residence time is in the order of 10^{-5} seconds, which is way lower than the nucleation time, so no liquid droplets will form and condensation will not occur.

6. Conclusions

A 1D analysis method for multistage centrifugal compressors consisting of two types of conventional loss models has been developed to examine and evaluate the conventional loss models for predicting performance of SCO_2 centrifugal compressors. The loss models are evaluated by comparing the 1D predicted results with experimental and 3D CFD results. Agreements and discrepancies are discussed in detail, and the main conclusions can be drawn as follows:

(1) The comparison of the 1D predicted results and the experimental data from SNL indicates that the combination of loss models adopted in the 1D analysis method in this study can well predict the pressure ratio of a single stage SCO_2 centrifugal compressor with vaned diffuser, but relatively large deviations of efficiencies reveal the deficiencies of the conventional models in predicting parasitic losses, in particular at a relatively

low flow rate. Under different operating conditions, the differences of pressure ratios tend to increase with increasing rotating speed and mass flow, and the maximum deviations of the static pressure ratio at impeller outlet and the total pressure ratio at diffuser outlet are 3.6% and −5.5%, respectively.

(2) For the multistage cases, the comparisons with the 3D CFD simulations indicate that it is the underestimation of the slip factor by the 1D model that results in a lower blade work coefficient, rather than the overestimation of the impeller outlet flow factor coefficient. The underestimation of the slip factor is also one of the reasons that result in lower pressure ratio curves than those predicted by CFD.

(3) The features of deviations between CFD and 1D results are obtained and analyzed. Generally, the 1D models appear to predict relatively higher losses in the impeller and the vaned zone of the return channel. For the individual losses, the 1D incidence loss model for the impeller may predict much lower losses than the CFD, but the total amount of the losses predicted by the skin friction and blade loading loss models is relatively higher, especially at flow rate lower than the design value. For the return channel vane, in comparison to the CFD results, the 1D model predicts a much larger increase of the incidence loss at high flow rate, causing larger decline of the efficiency and the pressure ratio curves. This difference is caused by the bigger value of the parameter "optimum flow inlet angle" predicted by the 1D incidence loss model, rather than the differences of the absolute flow angles at the vane inlet.

(4) Fluid condensation near the blade leading edge and the relevant losses cannot be predicted by 1D models at the current state, and new models should be developed to judge the onset of the condensation and to account for the resulting losses in further studies.

Acknowledgements

This work was supported by the National Key Research and Development Program of China (No. 2016YFB0600100), National Natural Science Foundation of China (No. 51506195), and the Collaborative Innovation Center of Major Machine Manufacturing in Liaoning.

References

[1] Can carbon dioxide replace steam to generate power. http://www.scientificamerican.com/article/can-carbon-dioxide-replace-steam-to-generate-power, 2015 (accessed on 4 Jun 2019).

[2] Nikolai P., Rabiyat B., Aslan A., et al., Supercritical CO_2: properties and technological applications - A review. Journal of Thermal Science, 2019, 28(3): 394–430.

[3] Feher E.G., The supercritical thermodynamic power cycle. Energy Conversion, 1968, 8: 85–90.

[4] Dostal V., Driscoll M.J., Hejzlar P., A supercritical carbon dioxide cycle for next generation nuclear reactors. Massachusetts Institute of Technology, 2004, 154(3): 265–282.

[5] Wright S.A., Radel R.F., Vernon M.E., et al., Operation and analysis of a supercritical CO_2 Brayton cycle. Sandia Report, No. SAND2010-0171, 2010.

[6] Motoaki U., Hiroshi H., Takashi Y., Demonstration test plant of closed cycle gas turbine with supercritical CO_2 as working fluid. Strojarstvo, 2010, 52(4): 459–465.

[7] Cha J.E., Bae S.W., Lee J., Cho S.K., et al., Operation results of a closed supercritical CO_2 simple Brayton cycle. The 5th International Supercritical CO_2 Power Cycles Symposium, San Antonio, USA, 2016.

[8] Pecnik R., Colonna P., Accurate CFD analysis of a radial compressor operating with supercritical CO_2. The 3rd International Supercritical CO_2 Power Cycle Symposium, Boulder, Colorado, 2011.

[9] Pecnik R., Rinaldi E., Colonna P., Computational fluid dynamics of a radial compressor operating with supercritical CO_2. ASME Paper No. GT2012-69640, 2012.

[10] Rinaldi E., Pecnik R., Colonna P., Steady state CFD investigation of a radial compressor operating with supercritical CO_2. ASME Paper No. GT2013-94580, 2013.

[11] Rinaldi E., Pecnik R., Colonna P., Numerical computational of the performance map of a supercritical CO_2 radial compressor by means of three-dimensional CFD simulations. ASME Paper No. GT2014-26966, 2014.

[12] Ameli A., Turunen-saaresti T., Backman J., Numerical investigation of the flow behavior inside a supercritical CO_2 centrifugal compressor. ASME Paper No. GT2016-57481, 2016.

[13] Hosangadi A., Liu Z., Weathers T., Ahuja V., et al, Modeling multiphase effects in CO_2 compressors at subcritical inlet conditions. Journal of Engineering for Gas Turbines and Power, 2019, 141(8): 081005.

[14] Galvas M.R., Fortran program for predicting off-design performance of centrifugal compressors. NASA TN D-7487, 1973.

[15] Aungier R.H., Mean streamline aerodynamic performance analysis of centrifugal compressors. Journal of Turbomachinery, 1995, 117: 360–366.

[16] Oh H.W., Yoon E.S., Chung M.K., An optimum set of loss models for performance prediction of centrifugal compressors. Proceedings of the Institution of Mechanical Engineers Part A Journal of Power & Energy, 1997, 211: 331–338.

[17] Monge B., Design of supercritical carbon dioxide centrifugal compressors. University of Seville, Seville,

Spain, 2014.

[18] Lee J., Lee J.I., Ahn Y., et al., Design methodology of supercritical CO_2 Brayton cycle turbomachineries. ASME Paper No. GT2012-68933, 2012.

[19] Conrad O., Raif K., Wessels M., The calculation of performance maps for centrifugal compressors with vane-island diffusers. Proceedings of the Twenty-fifth Annual International Gas Turbine Conference and Twenty-second Annual Fluids Engineering Conference, New Orleans, Louisiana, 1980.

[20] Jansen W., A method for calculating the flow in a centrifugal impeller when entropy gradients are present. Proceedings of Royal Society Conference on Internal Aerodynamics (Turbomachinery), 1967.

[21] Coppage J.E., Dallenbach F., Eichenberger H.P., et al., Study of supersonic radial compressors for refrigeration and pressurization systems. WADC report 55–257, 1956.

[22] Johnston J.P., Dean R.C., Losses in vaneless diffusers of centrifugal compressors and pumps. Journal of Turbomachinery, 1966, 88(1): 49–62.

[23] Lieblein S., Schwenk F.C., Broderick R.L., Diffusion factor for estimating losses and limiting blade loadings in axial-flow-compressor blade elements. NACA RM E53D01, 1953.

[24] Daily J.W., Nece R.E., Chamber dimension effects on induced flow and frictional resistance of enclosed rotating disks. ASME Journal of Basic Engineering, 1960, 82(1): 217–230.

[25] Qiu X., Mallikarachchi C., Anderson M., A new slip factor model for axial and radial impellers. ASME Paper No. GT2007-27064, 2007.

[26] Aungier R.H., Centrifugal Compressors: A strategy for aerodynamic design and analysis. ASME Press, New York, 2000.

[27] Span R., Wagner W., A new equation of state for carbon dioxide covering the fluid region from the triple-point temperature to 1100 K at pressures up to 800 MPa. Journal of Physical and Chemical Reference Data, 1996, 25(6): 1509–1596.

[28] Lemmon E.W., Huber M.L., Mclinden M.O., NIST reference fluid thermodynamic and transport properties—REFPROP, Version 9.0. NIST Standard Reference Database 23, National Institute of Standards and Technology, Gaithersburg, MD, 2010.